nature communications

Article

https://doi.org/10.1038/s41467-025-63018-9

Contact-dominated localized electric-displacement-field-enhanced pressure sensing

Received: 27 October 2024

Accepted: 1 August 2025

Published online: 29 August 2025

Check for updates

Chao Ma[1,5], Huaidong Ye[2,5], Xiaowei Shi[3,5], Yufan Chen[1,5], Yuxuan Liu[2], Longhui Qin[3], Lanyue Gan[1], Fan Xia[1], Guanhua Long[1], Xijun Jiang[2], Weicheng Huang[4], Xingxing Chen[1], Xuelei Liang[1], Lian-Mao Peng[1] & Youfan Hu[1]

Pressure sensors, especially the typical capacitive sensors that feature low power consumption, have drawn considerable interest in emerging and rapidly growing fields such as flexible electronics and humanoid robots, but often suffer from limited performance. Here, we report a contact-dominated design for capacitive pressure sensors to dramatically improve the sensing response and linearity over a broad pressure range. This design is implemented by utilizing hierarchical microstructured electrodes made of robust conductive composites with metallic coverage and layered dielectrics with high unit-area capacitance to realize localized electric-displacement-field-enhanced capacitance change. We demonstrate a significant improvement in pressure response beyond 3000 and a sensing range exceeding 1 MPa, particularly with a near-linear response (optimized R^2 of 0.9998) and high sensitivity of 9.22 kPa^{-1} in a wide pressure range of 0–100 kPa. Moreover, we present that the integration of the contact-dominated sensor with floating-gate low-dimensional semiconductor transistors can provide a transduced electrical response of ~4×10^5 at a low operating voltage of 2.66 V due to the greatly enhanced pressure response. We also demonstrate the potential applications of our sensor in fluid physical property evaluation and precise dynamic control of a robotic arm for manipulation tasks.

Over the past two decades, many endeavors have been committed to enabling the functionalization of humanoid robots, biomimetic prosthetics, human-machine interfaces, and diverse human-oriented future intelligent technologies to accurately and robustly detect various mechanical stimuli and interactions[1–3]. This has driven tremendous efforts in the design of high-performance flexible pressure sensors[4,5], and different sensing mechanisms have been explored, including piezoresistive[6–8], piezoelectric[9–11], optical[12,13], capacitive[14–16], iontronic[17,18], etc. Generally, piezoresistive pressure sensors are highly sensitive and easy to manufacture, but they have issues with temperature sensitivity and high power consumption. Piezoelectric sensors can be self-powered, but only respond to dynamic changes. Optical sensors also have high sensitivity and are not affected by temperature changes, but the device structure is usually more complex and more difficult to manufacture. Iontronic sensors achieve ultrahigh pressure response and sensitivity, but this

[1]Key Laboratory for the Physics and Chemistry of Nanodevices and School of Electronics, Peking University, Beijing, China. [2]Hunan Institute of Advanced Sensing and Information Technology, Xiangtan University, Xiangtan, Hunan, China. [3]School of Mechanical Engineering, Southeast University, Nanjing, China. [4]School of Engineering, Newcastle University, Newcastle upon Tyne, UK. [5]These authors contributed equally: Chao Ma, Huaidong Ye, Xiaowei Shi, Yufan Chen. e-mail: lmpeng@pku.edu.cn; youfanhu@pku.edu.cn

emerging class of pressure sensors usually faces challenges such as power consumption, stability, biocompatibility, and is more susceptible to changes in electric field frequency and temperature.

In this work, we focus on capacitive sensors, which have advantages such as low power consumption, minimal temperature dependence, and excellent stability[19,20], but usually suffer from limited sensitivity and poor linearity. The performance of a capacitive pressure sensor is generally governed by its mechanical and electrical dynamic characteristics, with the sensitivity being determined by the compressibility of the sensing element and the corresponding electrical response for a given deformation, i.e., the normalized capacitance change ($\Delta C/C_0$), where ΔC is the capacitance change under deformation and C_0 is the initial capacitance of the device. The creation of microstructures in elastomer dielectrics can lead to a reduced effective compressive modulus and a slightly increased effective dielectric constant, thereby offering an effective strategy to improve the sensitivity[21]. However, owing to the unstructured portion in the elastomeric dielectric that necessitates maintaining the microstructures and its relatively low dielectric constant, the electrical response $\Delta C/C_0$ based on this design is usually limited within 3[21–27]. Another strategy of utilizing microstructured electrodes[28–35] as sensing elements allows the use of dielectrics with smaller thickness and/or higher dielectric constant to reduce the effect from the unstructured portion in the elastomeric dielectric, leading to an increase in $\Delta C/C_0$ toward 40[32,34,35]. However, improvements in the wide-range sensitivity and linearity remain a critical challenge. Recently, by introducing compressible air gaps between the microstructured electrode and the dielectric layer, the response $\Delta C/C_0$ was further promoted to approximately 250[36]. Nevertheless, the very narrow sensitivity range (within 3 kPa) and nonlinear response significantly limit the application of this sensor in many scenarios (e.g., performing most routine manipulation tasks and measuring pressure when preloads are required)[34].

Transistor-based pressure sensing devices constructed by integrating capacitive pressure-sensitive elements with thin-film transistors (TFTs)[21,36–39] have the potential to develop high-performance compact functionalized flexible electronics since they can directly transduce capacitance changes into current variations and the sensitivity can be significantly increased by operating the transistor in the subthreshold regime[36,38]. However, previous demonstrations based on organic TFTs (OTFTs) with microstructured dielectrics[21,37,38] generally required a high operating voltage (>50 V) and yielded a limited transduced electrical response ($\Delta I/I_0 < 10^3$) due to the weak electrostatic control in microstructured dielectrics, low mobility, and relatively low current on/off ratio of OTFTs. By directly laminating pressure-sensitive gates of microstructured electrodes on high-performance two-dimensional (2D) semiconductor transistors with thin dielectrics[36], the operating voltage can be reduced to 20 V, but it is still not within a reasonable range.

Here, we report a contact-dominated localized electric-displacement-field-enhanced design strategy to significantly enhance the pressure response and linearity of capacitive sensors over a broad range. By utilizing hierarchical microstructured electrodes made of robust conductive composites with metal coverage, as well as layered dielectrics with a high unit-area capacitance, we achieve a pressure response $\Delta C/C_0$ exceeding 3000, more than an order of magnitude higher than the previous record[36], and a working range exceeding 1 MPa, with an optimum value of 2 MPa. In particular, the pressure sensors exhibit high linearity with an optimal R^2 value of 0.9998 and a high sensitivity of 9.22 kPa^{-1} in the pressure range of 0–100 kPa. We demonstrate that the contact-dominated design can be integrated with floating-gate low-dimensional semiconductor transistors, allowing full utilization of the on/off ratio of the transistor to further improve the pressure response at a low operating voltage of 2.66 V. We also show that our contact-dominated pressure sensors have potential for evaluating the physical properties of fluids and implementing manipulation tasks with precise dynamic control.

Results

Contact-dominated localized electric-displacement-field-enhanced design

Our design consists of two critical components: robust hierarchical microstructured electrodes made of conductive composite with metallic coverage, and dielectrics with a high capacitance per unit area, realized by utilizing thin and/or high-k layered dielectrics, as shown in Fig. 1a. According to the electric displacement field

$$D \propto \varepsilon_{\mathrm{diel}}/d_{\mathrm{diel}} \tag{1}$$

where $\varepsilon_{\mathrm{diel}}$ and d_{diel} are the relative dielectric constant and thickness of the dielectric layer, respectively, the simulation of the electric displacement field distribution in the microstructured electrodes in Fig. 1b and Supplementary Fig. 1a clearly reveals that increasing $\varepsilon_{\mathrm{diel}}$ and/or reducing d_{diel} can notably enhance the electric displacement field at the contact area between the microstructured electrode and the dielectric layer and thus locally increase the electric energy density (W_e) (Fig. 1c and Supplementary Fig. 1b) because

$$W_e = \frac{1}{2}DE \tag{2}$$

with E denoting the electric field. Considering that the capacitance (C) can be expressed as

$$C = 2\iiint_{\Omega} W_e \mathrm{d}\Omega/V^2 \tag{3}$$

where V and Ω denote the electric potential and volume of the dielectrics, respectively, the change in the capacitance in our sensor is thus dominated by the change in the capacitance at the contact area (termed the contact capacitance, C^{cont}) induced by the locally enhanced electric displacement field. In principle, any thin and/or high-k dielectric that provides a high capacitance per unit area is effective for our design. Here, we use layered dielectrics of 5-nm/50-nm-thick Y_2O_3/HfO_2 and 15-nm/200-nm-thick HfO_2/parylene fabricated on ultrathin substrates (Supplementary Fig. 2a) for the demonstration.

The utilization of hierarchical microstructures of micropyramids (Supplementary Fig. 2b) or self-patterned random rough surfaces (approximately regarded as a combination of microcones of multiple sizes) (Supplementary Fig. 2c) can not only introduce more air gaps before a pressure is applied (i.e., in the initial state) to reduce the initial capacitance (C_0) but also involve more contact regions and a continuous increase in the contact areas with increasing pressure over a greatly extended pressure range, ensuring a contact-dominated electrical response over a wide pressure range (Fig. 1d) and thus promising a larger capacitance change ($\Delta C \approx C^{\mathrm{cont}} - C_0$) than regular sensors[32,36]. Note that our microstructured electrodes are made of robust conductive composites (e.g., polydimethylsiloxane/carbon nanotubes (PDMS/CNTs)) and covered with a thin metallic layer that delivers a large effective conductive contact area under pressures to ensure a high contact-dominated response, which is further explained in the working mechanism section.

To highlight our contact-dominated design, we compared the normalized capacitance change with that of previous designs containing microstructures based on a highly simplified parallel plate capacitor model (Supplementary Note 1). For the microstructured dielectric design, the normalized capacitance change can be expressed as

$$\Delta C^{\mathrm{diel}}/C_0 \approx \Delta d_{\mathrm{air}}/(d_{\mathrm{air}} + k_{\mathrm{elas}}) \tag{4}$$

where Δd_{air} and d_{air} are the thickness change and the corresponding thickness of the air under a certain applied pressure, respectively; k_{elas} obeys $k_{\mathrm{elas}} \propto d'_{\mathrm{elas}}/\varepsilon_{\mathrm{elas}}$, with d'_{elas} and $\varepsilon_{\mathrm{elas}}$ being the unstructured

https://doi.org/10.1038/s41467-025-63018-9

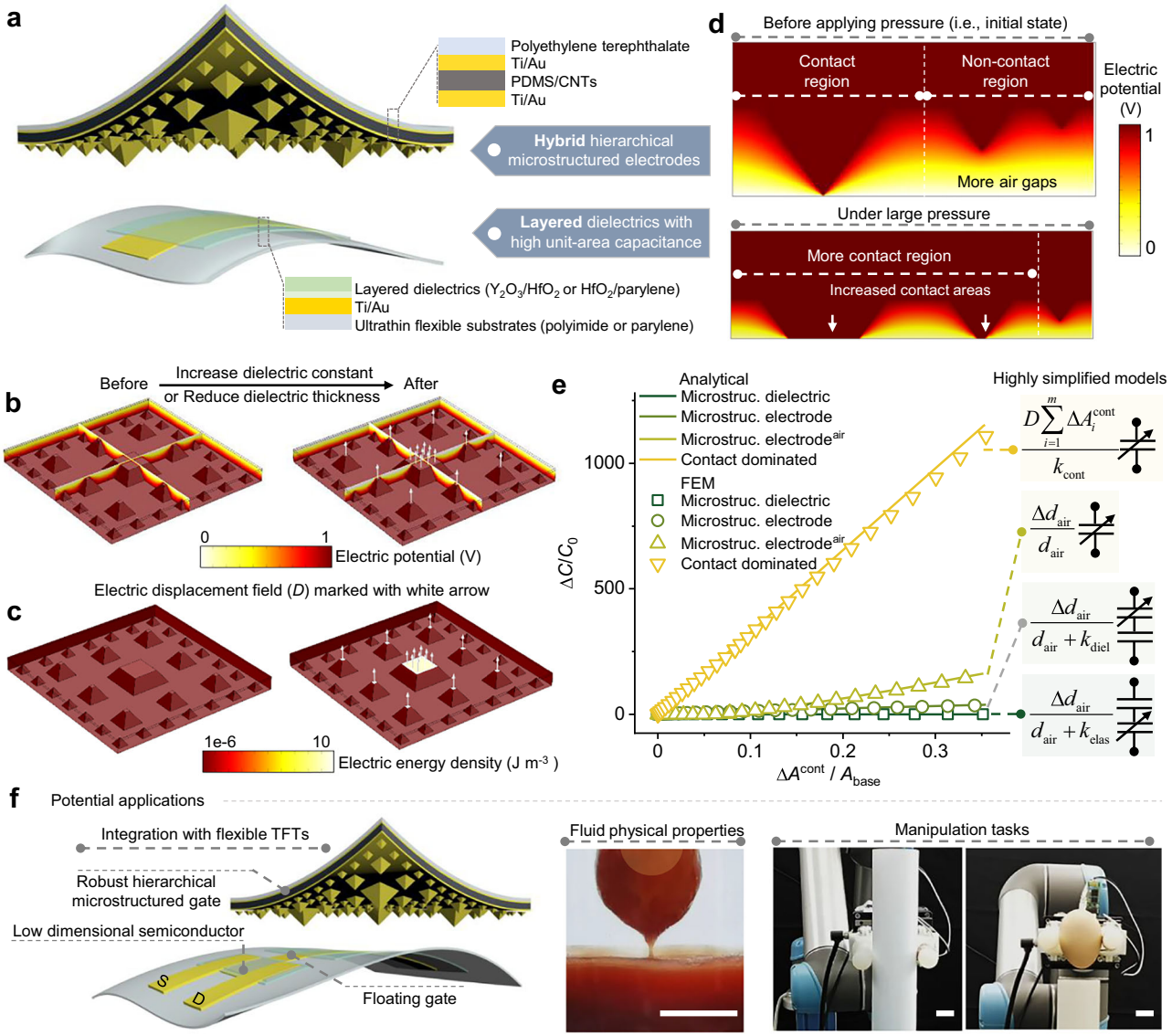

Fig. 1 | Principle, design, and potential applications of contact-dominated localized electric-displacement-field-enhanced pressure sensors. a Schematic of contact-dominated localized electric-displacement-field-enhanced capacitive pressure sensors (polydimethylsiloxane/carbon nanotubes, PDMS/CNTs). **b** Electric displacement field (marked with white arrows) and electric potential distributions in the hierarchical microstructured electrodes before (left) and after (right) increasing the dielectric constant or reducing the dielectric thickness. **c** Electric energy density and electric displacement field (marked with white arrows) distributions before (left) and after (right) increasing the dielectric constant or reducing the dielectric thickness. **d** Cross-sectional view of the electric potential distribution before applying pressure and under a high pressure. **e** Normalized capacitance change with the normalized contact area change ($\Delta A^{cont}/A_{base}$, where A_{base} is the area of the base surface of the microstructures) for a microstructured dielectric (microstruc. dielectric), a microstructured electrode (microstruc. electrode), a microstructured electrode with air gaps (microstruc. electrode^{air}), and our contact-dominated design (contact dominated) obtained via analytical models and finite element method (FEM) simulations. Right: the corresponding simplified circuit models. **f** Schematic of the integration of floating-gate low-dimensional thin film transistors (TFTs) with the contact-dominated design (left); our pressure sensors have the potential to evaluate the physical properties of fluids and enable robots to perform manipulation tasks (right), scale bar, 1.5 cm. Source data are provided as a Source Data file.

elastomer thickness and dielectric constant. The pressure response is notably limited by the thick and low-k unstructured elastomer layer (e.g., 1.2[21], 1.5[22], 2.5[23], 2.8[24], 2.5[25], 2.9[26], 1.4[27]). The normalized capacitance change for the microstructured electrode design can be written as

$$\Delta C^{elec}/C_0 \approx \Delta d_{air}/(d_{air}+k_{diel}) \quad (5)$$

where $k_{diel} \propto d'_{diel}/\varepsilon_{diel}$, with d'_{diel} and ε_{diel} being the dielectric thickness and dielectric constant, respectively. Typically, with this design, the dielectrics can be thinner and/or have a higher dielectric constant, resulting in an elevated electrical response (e.g., 20[32], 37[34], 30[35]). When compressible air gaps are introduced into the microstructured electrode design, the normalized capacitance change can be expressed as

$$\Delta C^{air-gap}/C_0 \approx \Delta d_{air}/d_{air} \quad (6)$$

with a greatly promoted value (e.g., approximately 250[36]) due to the reduced C_0.

The normalized capacitance change for our contact-dominated design can be described as

$$\frac{\Delta C^{cont}}{C_0} \approx \frac{D\sum_{i=1}^{m}\Delta A_i^{cont}}{k_{cont}} \quad (7)$$

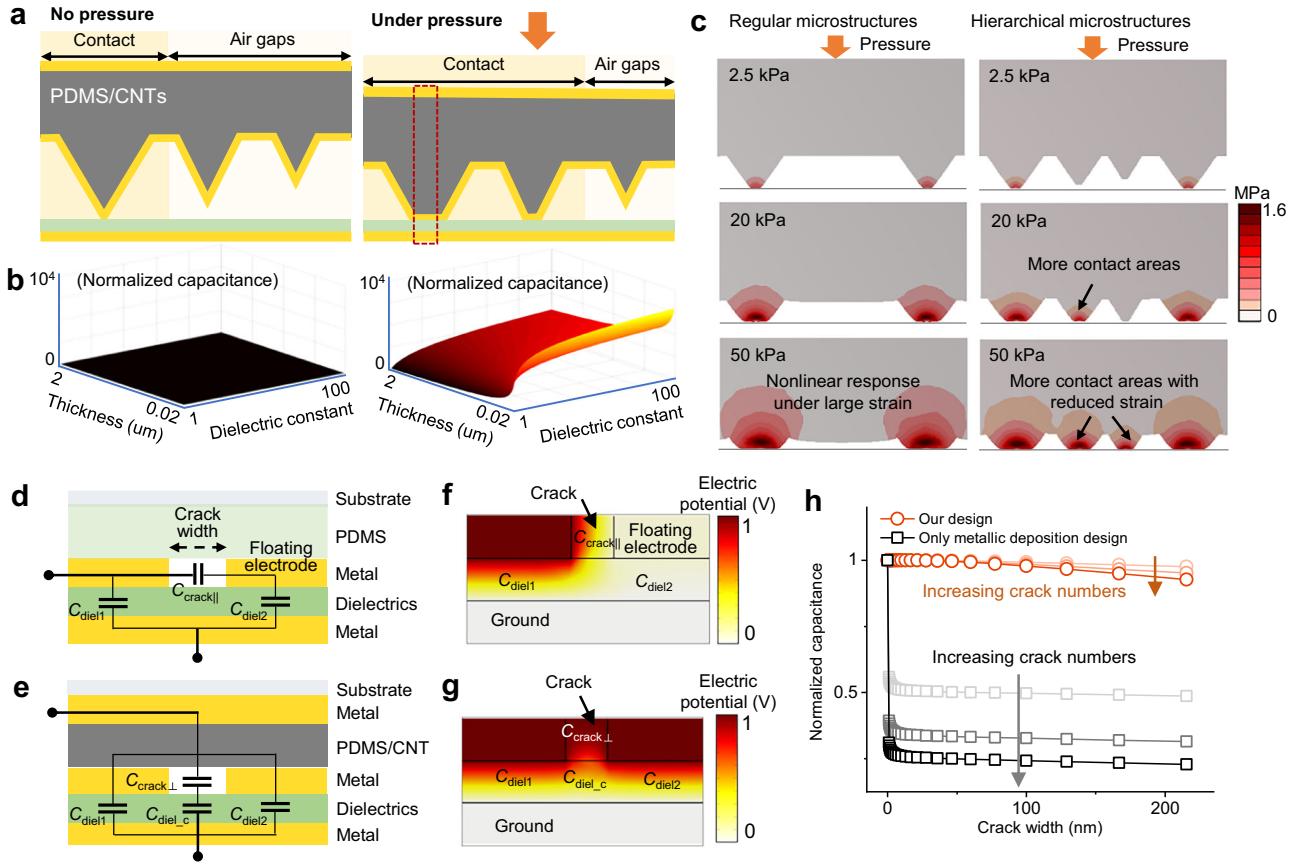

Fig. 2 | Working mechanism of contact-dominated localized electric-displacement-field-enhanced pressure sensors. a Schematics of the cross-sectional view of the contact-dominated pressure sensors without and with applied pressure. Red dashed box corresponding to the part represented by the schematic diagrams in (**e**). **b** Normalized capacitance (C/C_{min}, with C_{min} being the minimum value of the capacitance) with respect to the dielectric constant and thickness in the initial state (i.e., no pressure applied), left, and under pressure with $A^{cont}/A_{base} \approx 0.08$, right, obtained by analytical models. **c** Equivalent stress and strain distributions in regular and hierarchical microstructures under different pressures according to FEM simulations. Schematics and equivalent circuit diagrams for the only metal deposition design (**d**) and our hybrid electrode design (**e**) at the contact area when cracks occur. Corresponding electric potential distributions from FEM simulations for the only metal deposition design (**f**) and our hybrid electrode design (**g**). **h** Numerical results based on FEM simulations of the normalized capacitance for the only metal deposition design ($C_{all}^{metal}/C_{origin}$) and our hybrid electrode design ($C_{all}^{hybrid}/C_{origin}$) with respect to the crack width and crack numbers. The cracks are assumed to be uniformly distributed within the contact electrode. Source data are provided as a Source Data file.

where m is the number of contact regions, ΔA_i^{cont} is the change in the contact area in the ith contact region, and $k_{cont} \propto 1/d'_{air}$, with d'_{air} being the initial thickness of the air. The response for our design is dominated by the capacitance change at the contact areas and can be further enhanced by the electric displacement field. The more air gaps in the initial state (decreasing k_{cont}) and the more contact areas under high pressure (increasing m) induced by the hierarchical microstructures further improve the response. We also utilized analytical models (Supplementary Note 2) and finite element method (FEM) simulations (see **Methods** for the detailed parameters) to quantify the normalized capacitance change as a function of the normalized contact area change for these different designs (Fig. 1e), which shows that the $\Delta C/C_0$ for our contact-dominated design is significantly greater than that for the previous designs and has a good linearity over a wide range.

As illustrated in Fig. 1f, this contact-dominated design is feasible to integrate with low-dimensional semiconductor transistors, and can provide sensitive dynamic response for fluid physical property evaluation and enable robots to perform manipulation tasks through dynamic and accurate pressure feedback.

Working mechanism of the contact-dominated design

Figure 2a shows a schematic cross-sectional view of our contact-dominated pressure sensors without and with applied pressure. The initial capacitance C_0 of the sensor is determined primarily by the air gaps created by the hierarchical microstructured electrodes and has little dependence on the dielectric constant or thickness of the dielectric layer because of the limited contact regions and very small contact areas (left in Fig. 2b). However, as the contact areas increase, the capacitance under applied pressure can be significantly increased by increasing the dielectric constant and/or reducing the dielectric thickness (right in Fig. 2b) because the capacitance is dominated by the contact capacitance (i.e., $C \approx C^{cont}$).

According to contact mechanics[40,41], the applied pressure (P) for micropyramidal or microconical structures can be described as (Supplementary Note 3)

$$P \propto \frac{E_Y \tan\theta}{1-\nu^2} A^{cont} \tag{8}$$

where θ is the angle between the base and side surfaces of a micropyramid or a microcone; E_Y and υ are the Young's modulus and Poisson's ratio of the elastomeric microstructures, respectively. As θ and υ can be considered constant, the contact area A^{cont} is proportional to P when E_Y remains unchanged. However, the modulus of elastomers typically increases notably under large strains (i.e., in the nonlinear region)[42]. Compared with regular microstructures, the hierarchical design introduces additional contact areas under large pressures

through the small-sized microstructures, which effectively prevents large-sized microstructures from reaching large strains (i.e., the nonlinear region); meanwhile, the small-sized microstructures themselves usually operate under small strains (i.e., in the linear region) (Fig. 2c and Supplementary Fig. 3). Thus, the hierarchical design can guarantee a proportional relationship between the applied pressure and contact area over a wider pressure range, where the contact mechanics are the dominant mechanical behavior. Considering that the contact-dominated electrical response is also proportional to the contact area according to Eq. (8), our contact-dominated design thus ensures a linear pressure response over a broader range.

Given that the capacitance change of our sensor is dominated by the contact term, enhancing the portion of the effective conductive contact area (α) in the pressure-induced A^{cont} is critical to ensure a high response, which is achieved by creating hybrid microstructured electrodes made of conductive composites with metallic coverage. The metallic coverage solves the problem of limited effective conductive contact area (Supplementary Fig. 4) constrained by the conductive network nature of nanofillers in conductive composites[32] with greatly increased α, leading to a considerable improvement in the pressure response (Supplementary Fig. 5). When only a thin metal layer is deposited on the surface of a microstructured elastomer[36], cracks are usually formed, especially under high strain/stress, due to mechanical mismatch (Supplementary Fig. 6), which can be referred to as floating electrodes. The overall capacitance C_{all}^{metal} is significantly lower than the original capacitance without cracks (C_{origin}) because of the newly generated parallel connected capacitor branch, which includes two serially connected capacitors, $C_{crack||}$ and C_{diel2}, as shown in Fig. 2d, where $C_{crack||}$ is the capacitor generated horizontally across the crack and C_{diel2} (C_{diel1}) is the capacitor between the floating electrode (electrode) and the ground. As $C_{crack||} << C_{diel2}$, assuming that n cracks are uniformly generated, C_{all}^{metal} will decrease to $C_{all}^{metal} \approx C_{origin}/(n+1)$ (Supplementary Note 4.1). In contrast, our hybrid electrode design provides robust conductive paths to bridge floating electrodes to dramatically reduce the effects of cracks. As shown in Fig. 2e, three parallel connected capacitor branches are constructed in this case, and

$$C_{all}^{hybrid} = C_{diel1} + C_{diel2} + \frac{C_{crack\perp} C_{diel\_c}}{C_{crack\perp} + C_{diel\_c}} \quad (9)$$

in which $C_{crack\perp}$ is the capacitor generated vertically across the air gap and C_{diel_c} is the capacitor generated vertically across the dielectric underneath the air gap. Since $C_{crack\perp}$ and C_{diel_c} are generally very small due to the narrow crack width, the contribution of these branches to the total capacitance is minimal, resulting in $C_{all}^{hybrid} \approx C_{origin}$ (Supplementary Note 4.2). The simulation of the electric potential distribution for the case of only metallic deposition (Fig. 2f) clearly reveals that the electric potential gradient (∇V) between the floating electrode and ground is significantly reduced due to the presence of cracks, indicating a greatly reduced capacitance according to $\nabla V \propto E \propto C$. In contrast, the electric potential in our hybrid design (Fig. 2g) is essentially uniformly distributed in the dielectrics, with little effect from cracks. Our numerical results based on the FEM (Fig. 2h) also show that, compared with the only metallic deposition design, our hybrid design could greatly minimize the capacitance reduction induced by increased number and width of cracks, thus ensuring a high electrical response (Supplementary Fig. 7). To verify the robustness of the hybrid microstructured electrode, the hybrid microstructured electrode was subjected to bending, folding, pressing, and stretching conditions, and then the pressure response of the sensor with the hybrid microstructured electrode and layered dielectric of HfO_2/parylene was examined. It can be observed from Supplementary Fig. 8 that pressure responses of the sensor exhibit good robustness after these mechanical processes, which indicates that, with the hybrid microstructured electrode design, even if cracks formed during these processes, they have little effect on the pressure response of our sensors.

Performance of the contact-dominated pressure sensors

An ultrahigh $\Delta C/C_0$ of ~3327 over a broad dynamic range of 1 MPa is demonstrated by using a self-patterned hierarchical microstructured electrode and layered dielectrics of 5-nm/50-nm-thick Y_2O_3/HfO_2 (Fig. 3a). In general, the sensitivity of capacitive pressure sensors is defined as

$$S = \delta(\Delta C/C_0)/\delta P \quad (10)$$

At a pressure of 1 MPa, our sensor holds a sensitivity of 1.13 kPa^{-1}; in the pressure range of 0–100 kPa, our pressure sensor has a high sensitivity of 9.22 kPa^{-1} (Fig. 3b), which is more than one order of magnitude greater than that of the state-of-the-art sensors (e.g., 0.68 kPa^{-1} [32], 0.7 kPa^{-1} [34], 0.15 kPa^{-1} [35]) in similar pressure ranges, and in the low-pressure range of 0–10 kPa, the sensitivity is 11.12 kPa^{-1} (inset of Fig. 3b), which exceeds that of most typical capacitive sensors in the low-pressure regime[21–27]. Our pressure sensor also delivers a high linearity of $R^2 = 0.9996$ in the low-pressure regime and $R^2 = 0.9980$ in the range of 0–100 kPa. Note that these characteristics can be readily tuned to meet different application requirements. A greater linearity ($R^2 = 0.9998$) in the wide range of 0–100 kPa can be obtained by using a more rigid elastomer (e.g., a 5:1 ratio of the PDMS base polymer to the curing agent) (Fig. 3c), and a larger dynamic range (2 MPa) can be achieved by employing layered dielectrics of 15-nm/200-nm-thick HfO_2/parylene with optimized mechanical and electrical robustness (Supplementary Fig. 9). Our design strategy is also effective for obtaining sensitive and linear pressure responses in both the low- and medium-pressure regimes using hierarchical pyramidal microstructures (Supplementary Fig. 10). Comparing with that of previous designs containing microstructures[21–27,43–63], as shown in Fig. 3d, the response $\Delta C/C_0$ of our sensor surpasses the previous record achieved with microstructured electrodes with air gaps[36] by one order of magnitude and is two to three orders of magnitude greater than those obtained with microstructured dielectrics and electrodes[21–38]. Additionally, our sensors deliver a working range of 1–2 MPa, which exceeds that of all the previous designs. Such a wide working range enables the sensor to clearly record the physical activities even under large pressures (more than 1 MPa), as shown in Supplementary Fig. 11, which indicates the great potential for applications in high-pressure scenarios.

We further investigated the effect of dimensional parameters and distribution of hierarchical micropyramids in microstructure electrodes on sensing performance. In general, the pressure response of our sensor is determined by both the mechanical compressibility of the hierarchical microstructures and the corresponding electrical response for a given deformation (i.e., the initial capacitance and the contact-dominated capacitance under pressures). The pressure response and sensitivity can be enhanced by increasing the spacing of the micropyramids due to the reduced initial capacitance and enhanced compressibility from the reduced density of micropyramids (Supplementary Fig. 12a, b). The increase in hierarchy of micropyramids can introduce more air gaps to reduce the initial capacitance and provide more contact areas as pressure increases over a wider pressure range, thereby leading to an increase in pressure response and sensitivity (Supplementary Fig. 12c, d). By increasing the size and height of micropyramids, the pressure response and sensitivity are enhanced due to the reduced initial capacitance and increased compressibility (Supplementary Fig. 13). The detailed pattern of the initial capacitance varying with the dimensional parameters and distribution

https://doi.org/10.1038/s41467-025-63018-9

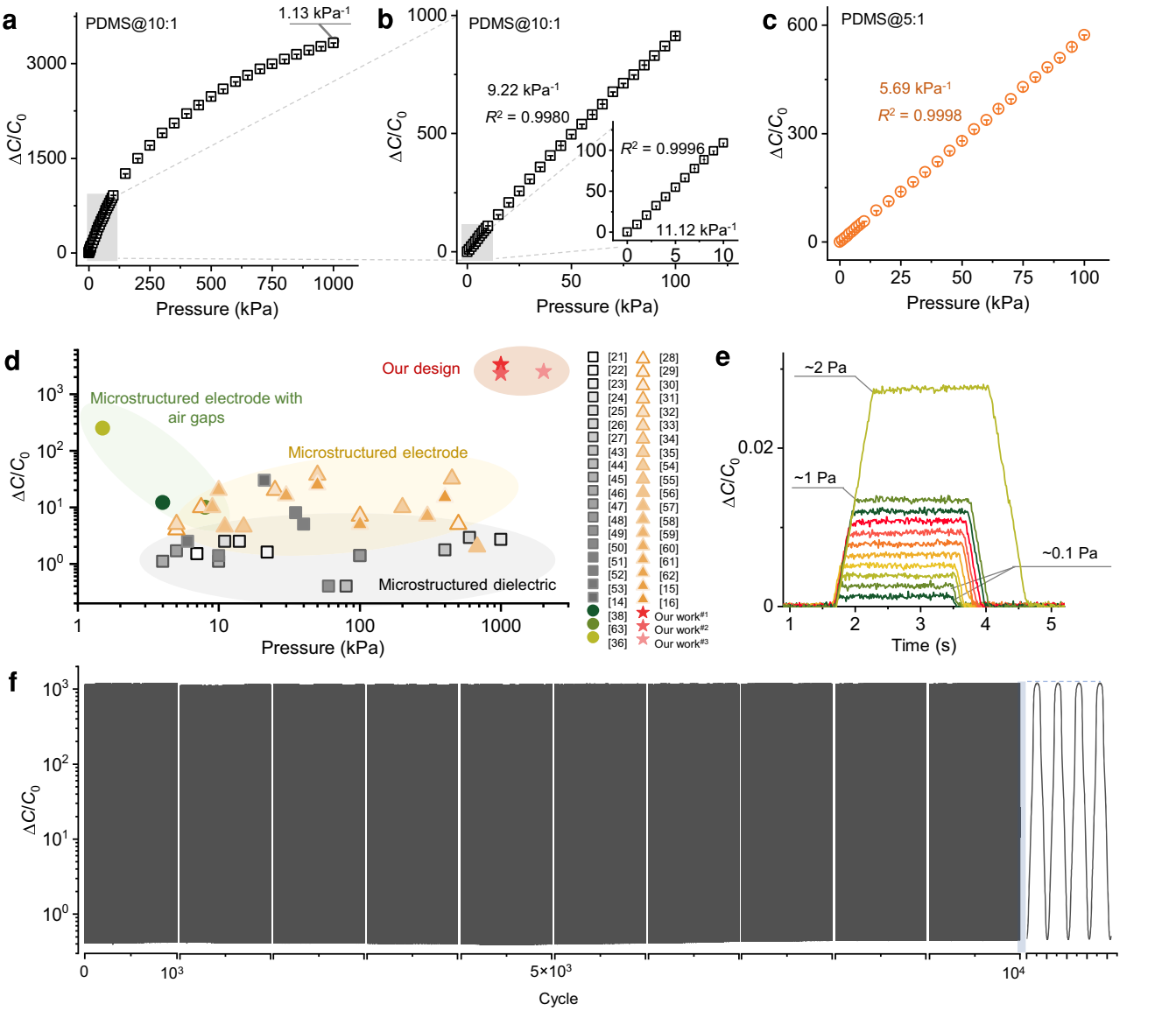

Fig. 3 | Performance of the contact-dominated pressure sensors. **a**–**c** Normalized capacitance change versus pressure for the sensor with self-patterned hierarchical microstructured electrodes and dielectrics of 5-nm/50-nm-thick Y_2O_3/HfO_2 (PDMS@10:1 and PDMS@5:1denote that the ratio of the PDMS base polymer to the curing agent is 10:1 and 5:1, respectively). The measure of center denotes the mean value, and the error bars indicate the standard deviation from 20 repeated measurements. **a** The employment of PDMS@10:1 for the range of 0–1 MPa and **b**, zoomed-in image of **a** for the range 0–100 kPa and inset of **b** for the range of 0–10 kPa. **c** The employment of PDMS@5:1 for the range of 0–100 kPa to obtain higher linearity. **d** Comparison of the pressure response with that of previous design strategies (our work[#1] and our work[#2] denote the employment of PDMS@10:1 and PDMS@5:1 with dielectrics of 5-nm/50-nm-thick Y_2O_3/HfO_2, respectively; our work[#3] denotes the employment of PDMS@10:1 with dielectrics of 15-nm/200-nm-thick HfO_2/parylene). **e**, Pressure response at small pressures. Our sensor can resolve one-tenth of the normalized capacitance change at ~1 Pa (i.e., ~0.1 Pa). **f** Mechanical stability test under cyclic compression at ~100 kPa over 10^4 cycles, with a zoom-in of 4 cycles (right). Source data are provided as a Source Data file.

of hierarchical micropyramids in microstructure electrodes is summarized in Supplementary Fig. 14.

To characterize the flexibility of the layered dielectrics, different bending tests were performed on them, and then the pressure response of the sensor with the layered dielectric was examined, which exhibited good mechanical reliability as shown in Supplementary Fig. 15. We note that the layered dielectric of HfO_2/parylene containing thinner HfO_2 can provide higher flexibility than layered dielectric of Y_2O_3/HfO_2 due to the reduced bending stiffness. To evaluate the pressure response of the sensor under bending conditions, we mounted the device on semi-circular glass substrates with curvature radii of 15 mm and 20 mm, respectively. As shown in Supplementary Fig. 16, the pressure response exhibits relatively small changes under these bending conditions. Note that specialized calibration may be needed when the bending radius is further reduced. Additionally, our sensors exhibit good stability after long-term storage, as shown in Supplementary Fig. 17.

Our design also enables the sensor to resolve a tiny pressure change of 0.1 Pa within an ultralow pressure range of 1 Pa (Fig. 3e). The sensor offers a fast response time of ~15 ms and a relaxation time of ~12 ms under a pressure of ~5 kPa (Supplementary Fig. 18). The cyclic performance at a pressure of 100 kPa for more than 10^4 cycles demonstrates the excellent mechanical robustness of our sensor (Fig. 3f). A detailed comparison of the sensing performance with other typical capacitive pressure sensors is shown in Supplementary Table 1. Note that the pressure

https://doi.org/10.1038/s41467-025-63018-9

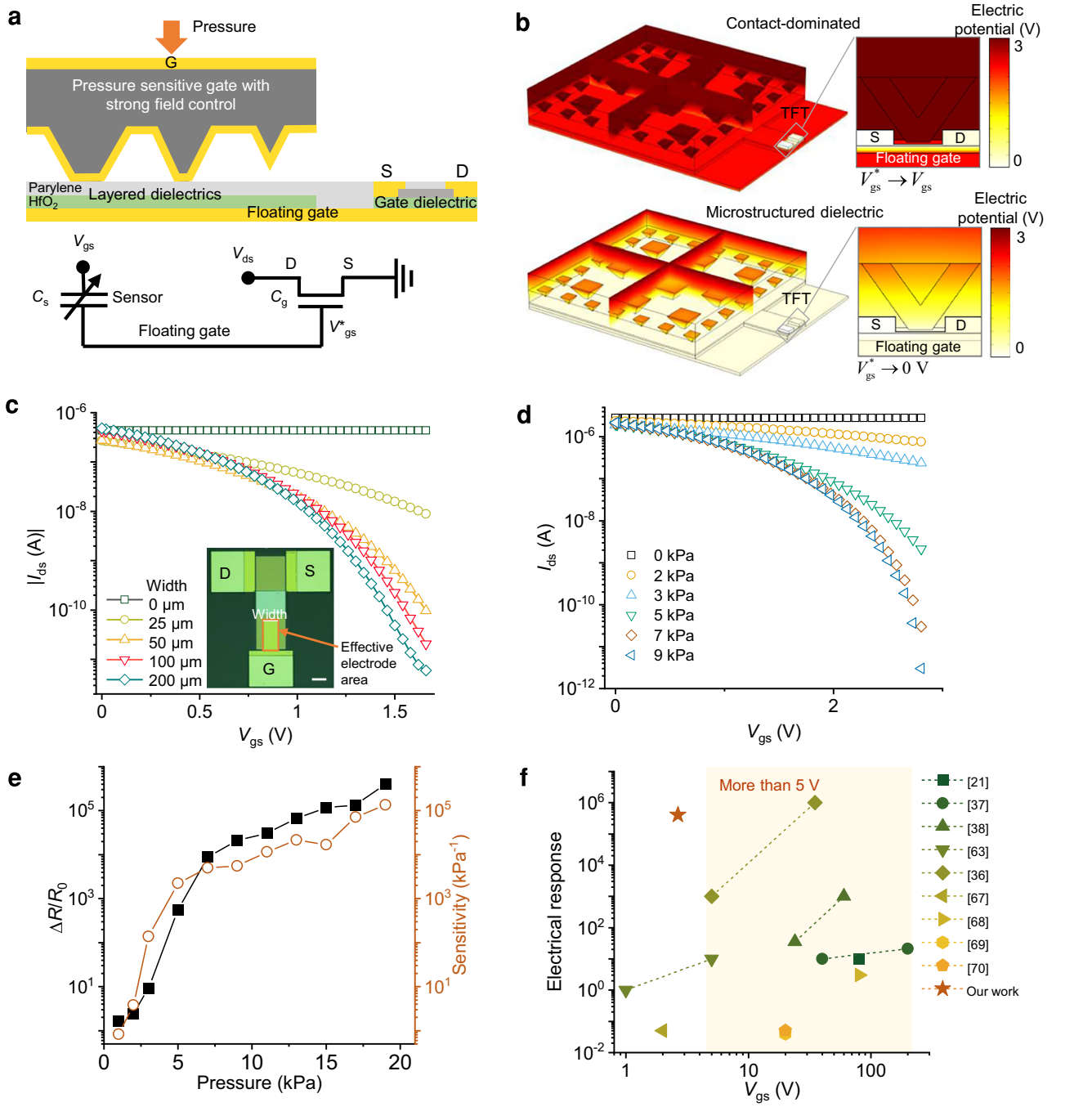

Fig. 4 | Integration of the contact-dominated design with low-dimensional transistors. a Schematics of the cross-sectional view of the integrated construction (top) and the equivalent circuit diagram (bottom). **b** Electric potential distributions obtained via FEM simulations in the integrated sensors using our contact-dominated design and in the microstructured dielectric design with the same geometry under the same deformation. **c** Transfer curves of the CNT-based TFTs on a polyimide substrate at $V_{ds} = -0.1$ V with the same length but different widths of the effective gate electrode (i.e., different effective gate electrode areas). Inset: optical image of a TFT, scale bar, 50 μm. **d** Transfer curves of the integrated sensor at $V_{ds} = -0.5$ V under different pressures. **e** Normalized resistance change and corresponding sensitivity of the integrated sensor at $V_{ds} = -0.5$ V and $V_{gs} = 2.66$ V. **f** Comparison of the electrical response regarding to V_{gs} with that in previous reports on integrated capacitive pressure sensors. Source data are provided as a Source Data file.

responses based on our contact-dominated design show little dependence on the electrical frequency (Supplementary Fig. 19) and temperature (Supplementary Fig. 20), which is difficult to be achieved in iontronic sensors[64] that typically have a high response. The signal shifts are less than 0.02 kPa K^{-1} at 40 °C and less than 0.04 kPa K^{-1} even at 120 °C, which are considerably smaller than those in the previous reports: 0.3 kPa K^{-1} [21], 4.3 kPa K^{-1} [65] and 64 kPa K^{-1} [66] within 40 °C.

Integration with flexible low-dimensional transistors

Low operating voltages are highly desirable for integrated pressure sensors considering their power consumption, compatibility with portable power sources and wearable safety. However, a decreased operating voltage generally results in a considerable sacrifice of the sensing performance. Here, we integrated our contact-dominated sensor with low-dimensional semiconductor transistors (e.g., CNT-based TFTs) via a floating gate structure, as shown in Fig. 4a. The

floating gate voltage on the TFT (V^*_{gs}) can be expressed as

$$V^*_{gs} = \frac{C_s}{C_s + C_g} V_{gs} \tag{11}$$

where V_{gs} is the gate voltage applied on the sensing element and C_s and C_g denote the capacitances of the sensor and the gate dielectric, respectively. Thus, the change in the floating gate voltage ΔV^*_{gs} can be described as

$$\Delta V^*_{gs} = \frac{\Delta C_s}{C_g} \frac{V_{gs}}{(1 + C_s/C_g)^2} \tag{12}$$

This equation indicates that a large capacitance change ΔC_s in the sensing element enables a notable change in ΔV^*_{gs}, resulting in strong modulation of the TFT, which allows the integrated sensor to operate at lower voltages. We also simulated the electric potential distribution in the integrated sensor upon deformation by using our contact-dominated design and the microstructured dielectric design for comparison, as shown in Fig. 4b. The V^*_{gs} on the TFTs with our design approaches the applied V_{gs}, which is much larger than that (close to 0 V) obtained when using the microstructured dielectric design under the same deformation, indicating that our design has the potential to provide an enhanced transduced response with a dramatically reduced V_{gs} in the integrated sensor.

We first examined the transfer curves of floating-gate CNT-based TFTs with different effective gate electrode areas to simulate the contact area changes of our pressure-sensitive hierarchical electrodes in the integrated sensor under various pressures. Figure 4c shows that the source–drain current I_{ds} decreases as the effective gate electrode area increases at the same gate voltage. The transfer curves of our integrated sensor under different pressures are presented in Fig. 4d, which exhibit trends similar to those of the TFTs with different effective gate-electrode areas. In particular, an electrical response ($\Delta R/R_0$, where ΔR is the resistance change and R_0 is the initial resistance of the integrated sensor) of ~4×10^5 is achieved with our integrated sensors at a gate voltage of 2.66 V (Fig. 4e), which basically exploits the full range of the on-off ratios of the TFTs (Supplementary Fig. 21) and yields high sensitivities ($S = \delta(\Delta R/R_0)/\delta P$) of ~$5 \times 10^3 - 1.3 \times 10^5$ kPa^{-1} in the sub-threshold regime. Compared with previous reports[21,36–38,63,67–70], our device can enable a substantial decrease in the operating voltage to less than 3 V while providing greatly enhanced sensing performance (Fig. 4f). Furthermore, our design, which uses a floating gate and a layered dielectric, promises a larger pressure working range than the design of a microstructured electrode with air gaps, in which the sensitive electrode is directly laminated onto a very thin dielectric on a semiconductor prone to gate leakage, yielding a limited pressure range of less than 2.5 kPa[36]. In addition, our TFTs retain their electrical performance when bent to a small radius (Supplementary Fig. 22), indicating good mechanical stability.

Fluid physical property evaluation

Our contact-dominated sensor with a sensitive dynamic response is promising for many applications, including fluid pressure monitoring. We equipped a robotic arm with our sensor, which was attached to a rubber cylinder and connected to a readout circuit with a wireless module (Fig. 5a). The readout circuit (Supplementary Fig. 23) can convert the capacitance into the oscillation frequency of a square wave (Supplementary Fig. 24). Note that the oscillation frequency also exhibits a high linearity ($R^2 = 0.9989$) in the pressure range of 0–100 kPa (Fig. 5b) because of the linear response of our sensor with little frequency dependency. We conducted cyclic tests in which the sensor was immersed in various liquids and held at the same height, and then extracted from these liquids, including water, detergent, yogurt and honey. The dynamic responses of our sensor in different liquids exhibit distinctive features (Fig. 5c), which potentially enable evaluation of their physical properties.

Considering that the hydrostatic pressure exerted by a static fluid at a given point is determined by

$$P = \rho g h \tag{13}$$

where ρ is the density of the fluid, g is the gravitational acceleration, and h is the depth, the density of the fluid could be estimated by the measured pressure change between the initial and immersion states. To decouple the potential effect of different dielectric constants of the fluids, we packaged our sensor using thin metallic biaxially-oriented polypropylene (BOPP) film to shield the fringe fields (Supplementary Fig. 25). Figure 5d shows that the measured pressure change after decoupling the effect of the dielectric constant is essentially proportional to the fluid density and exhibits good linearity (Supplementary Fig. 26). In addition, the amount of fluid remaining on the sensor estimated by the pressure change between the initial and taken-out states after decoupling the effect of the dielectric constant may be related to the wettability and viscosity of the fluid. For example, detergents are usually slightly denser than water, but their wettability and viscosity are greatly enhanced by the small amounts of surfactants present in them[71], which is consistent with our experimental results that the residual detergent amount estimated by our sensor is significantly greater than that of water (Fig. 5e and Supplementary Fig. 27). We note that during further relaxation, the amount of fluid remaining on the sensor may be a result of competition between gravity, wettability and viscosity, which may result in less honey (denser but with lower wettability) residue than detergent at the end of the relaxation process (Supplementary Fig. 28).

Our sensors can record tiny pressure changes during dynamic processes to reveal more mechanically relevant fluid properties. Figure 5f shows the dynamic response and optical images captured during a dynamic process when the sensor is immersed in and removed from the fluid of ketchup. A sudden increase in the response is observed at the 2nd and 5th marked time points corresponding to the 2nd and 5th images, which can be attributed to the formation of a liquid bridge due to the surface tension of the fluid. Furthermore, a tiny increase is recorded at the 3rd time point, corresponding to the 3rd image, where the liquid bridge is broken.

Accurate dynamic control for manipulation tasks

Our contact-dominated sensor with accurate dynamic pressure feedback holds great potential in robotic applications for manipulation tasks. We employed two rubber cylinders installed on a gripper controller to grasp objects, one of which was integrated with our sensor connected to readout circuits (Fig. 6a). The pressure signals detected by the sensor can be wirelessly transmitted to control the speed or motion of the gripper via an adaptive algorithm (Supplementary Note 5), thereby performing manipulation tasks with controllable pressures. Our sensor-equipped robotic gripper can stably grasp various items, including cotton, rolled-up A4 paper, a ping pong ball and a scrub sponge (Fig. 6b). The applied grasping pressure can be precisely controlled based on the stiffness of the object, as evaluated algorithmically by our sensors (e.g., the pressure applied on cotton is lower than that applied on rolled-up A4 paper and is more than an order of magnitude lower than that applied on a ping-pong ball). We note that such accurate control enables the gripper to provide sufficient pressure to hold objects while almost retaining their original shapes, especially for soft objects, such as cotton and rolled-up A4 paper (Supplementary Movies 1 and 2). We note that when grasping items with high dielectric constant or conductive media (Supplementary Fig. 29), it may be necessary to package the device with a conductive film to eliminate fringe field-induced response.

https://doi.org/10.1038/s41467-025-63018-9

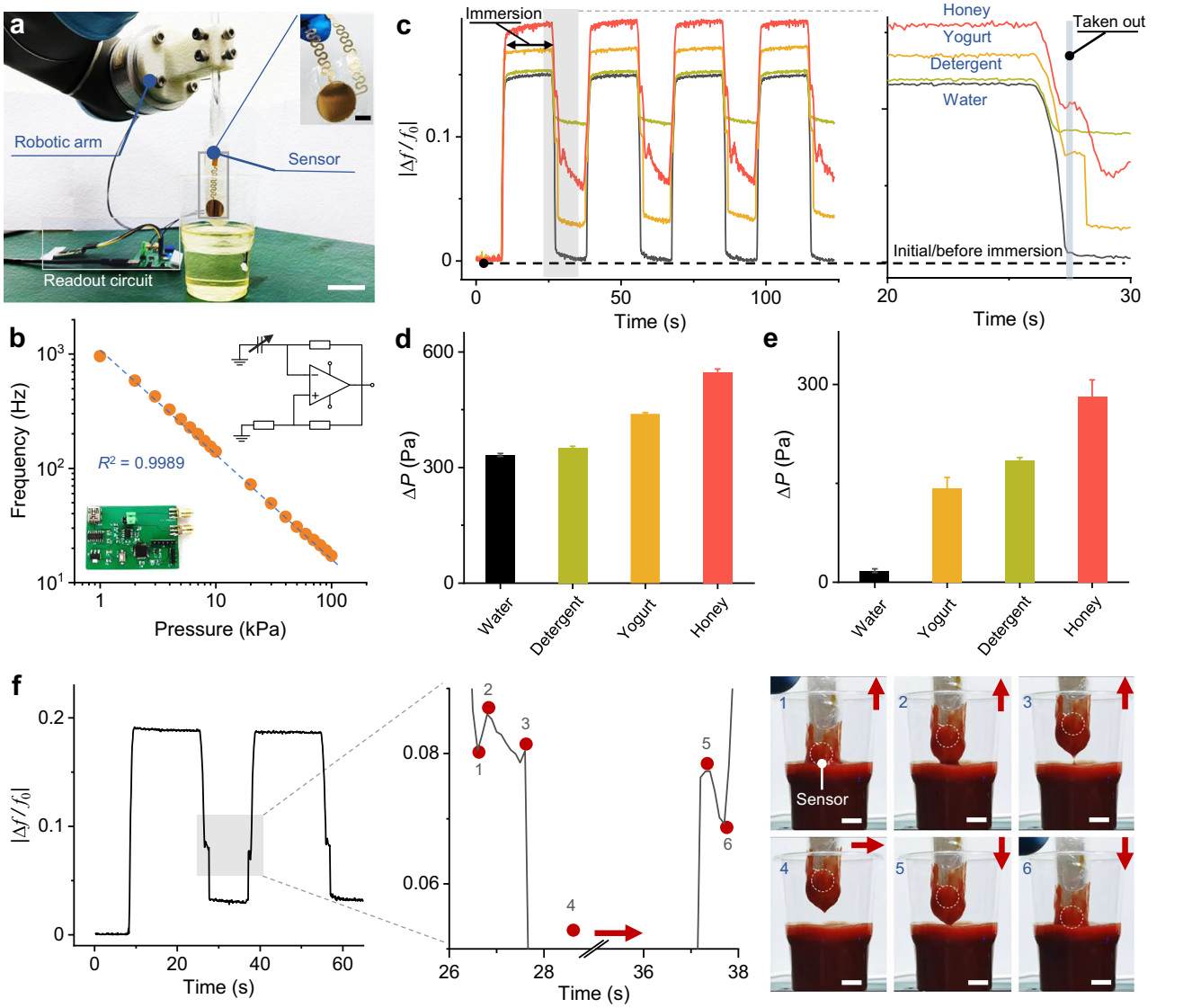

Fig. 5 | Potential applications in fluid physical property evaluation. **a** Photograph of the sensor-equipped robotic arm with readout circuits for the application, scale bar, 2 cm. Inset: photograph of the sensor, scale bar, 0.5 cm. **b** Oscillation frequency of the sensor after conversion as a function of pressure. Inset: diagram of the readout circuit and photograph of the readout module. **c** Cyclic tests of the dynamics of the normalized frequency change, where Δf is the recorded frequency change during this process and f_0 is the initial recorded frequency of the sensor, involve being immersed and held in, and extracted from various fluids. The zoom-in (right) clearly shows the taken-out state, which is defined as the point when the sensor is just extracted from the fluid. **d**, Measured pressure change between the initial and immersion states after decoupling the effect of the dielectric constant, which is almost proportional to the density (water: ~1 g/mL; detergent: ~1.05 g/mL; yogurt: ~1.2 g/mL; honey: ~1.4 g/mL). The measure of center denotes the mean value, and the error bars indicate the standard deviation from 100 repeated measurements. **e** Measured pressure change between the initial and taken-out states after decoupling the effect of the dielectric constant. The measure of center denotes the mean value, and the error bars indicate the standard deviation from 20 repeated measurements. **f**, Dynamics of the normalized frequency change of the sensor when it is immersed and held in and removed from ketchup. The zoom-in (middle) clearly shows the small variations in pressure, and corresponding optical images (right) of the position of the sensor, scale bar, 1 cm. Source data are provided as a Source Data file.

Our sensor-controlled robotic gripper can also grasp and hold objects even when slipping or perturbation occurs. We employed the gripper to grasp and lift a bottle filled with water (Fig. 6c) and then release it to allow the bottle to slide. Figure 6d shows the dynamics of the pressure change and controlled speed of the gripper during the process. A stable pressure signal can be observed with some small pressure change, which triggers minor adjustments of the gripper to ensure a stable grasp on the bottle. In particular, precise dynamic control enables the gripper to adaptively regrasp the bottle when it slips (Supplementary Movie 3). Vibrations of the robot can be observed when the gripper holds the bottle (Supplementary Movie 4), and our sensor can even resolve these vibrations, with a high-pressure resolution of 0.58% at ~8.6 kPa (Fig. 6e), which is more than an order of magnitude higher than that of human skin (7%)[72]. We also used the gripper to grasp, lift, and put down a measuring cylinder containing water (Fig. 6f), adding 2 mL of water twice during the process. Figure 6g shows that the precise dynamic feedback of our sensor enables the gripper to gradually apply increasing pressure to steadily hold the cylinder during perturbations, such as the addition of 2 mL of water and the actions of moving it down and putting it down (Supplementary Movie 5). The ability to detect tiny pressure changes enables the identification of contact force modes. When the sensor is gently pressed and then slid on different substrates, the time-frequency maps obtained by processing the sensor signals with the continuous wavelet transform algorithm[73] reveal obvious frequency-domain differences between pressing and sliding

https://doi.org/10.1038/s41467-025-63018-9

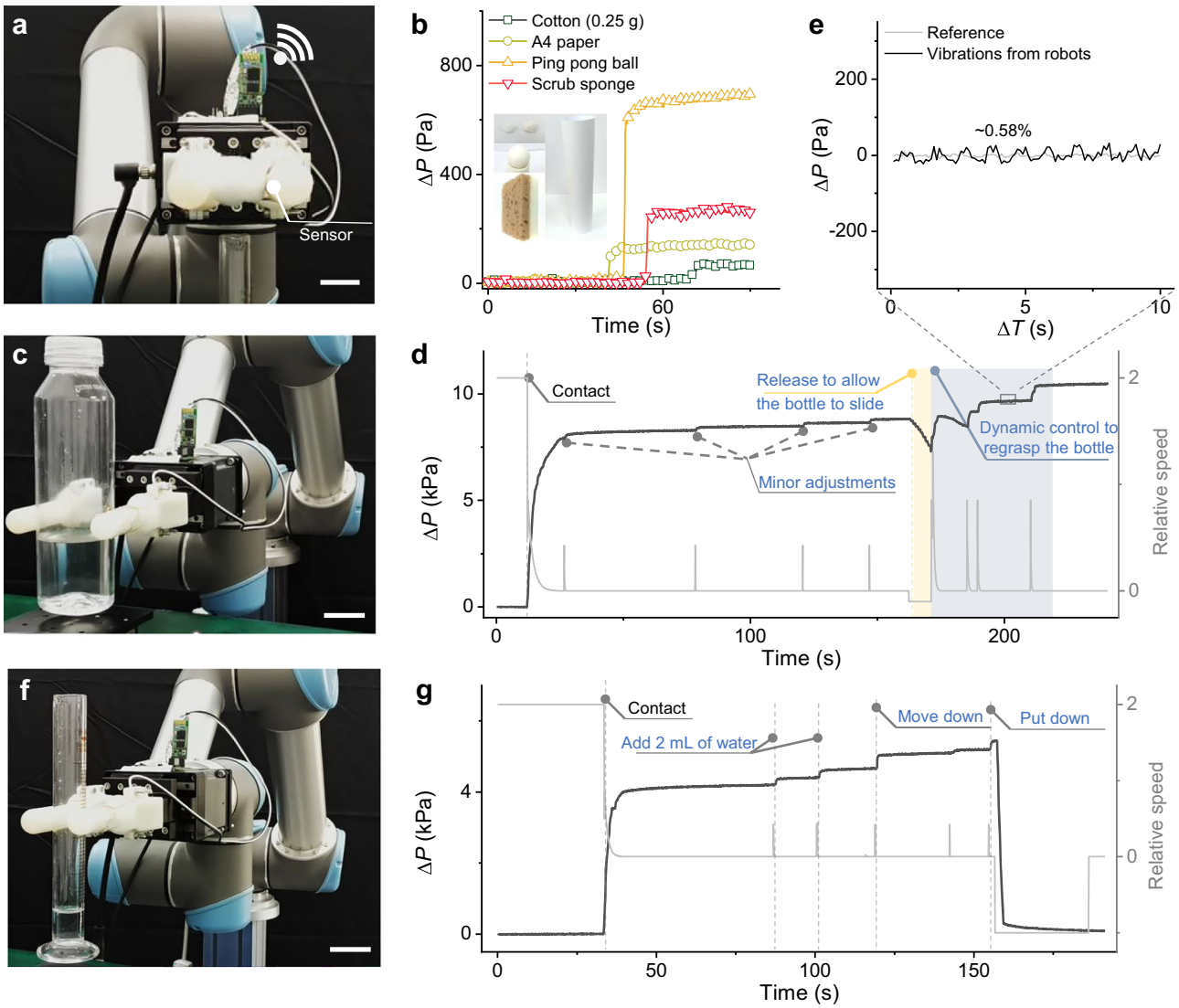

Fig. 6 | Potential applications in accurate dynamic control for manipulation tasks. a Photograph of the sensor-equipped robotic gripper grasping cotton, scale bar, 1.5 cm. **b** Dynamics of the pressure change when various objects are grasped. Inset: pictures of the objects, including cotton, rolled-up A4 paper, a ping pong ball and a scrub sponge. **c** Photograph of the sensor-equipped robotic gripper grasping a bottle containing water, scale bar, 3 cm. **d** Dynamics of the pressure change and controlled speed of the gripper during grasping and lifting of the bottle and when slipping occurs. **e** Measured pressure change induced by robot variations at a pressure of ~8.6 kPa detected by our sensor. **f** Photograph of the sensor-equipped robotic gripper grasping a measuring cylinder filled with water, scale bar, 3 cm. **g** Dynamics of the pressure change and controlled speed of the gripper when the measuring cylinder is grasped, 2 mL of water is added twice, and the cylinder is then put down. Source data are provided as a Source Data file.

on different substrates (Supplementary Fig. 30), allowing effective state discrimination and slip detection in robotic applications.

Discussion

We propose a contact-dominated localized electric-displacement-field-enhanced design strategy to achieve capacitive sensors with superior response and linearity over a broad pressure range. We show that our contact-dominated design with floating-gate transistors enables the integrated sensor to fully exploit the range of on/off ratios with enhanced sensing performance at a low operating voltage. Our design allows a wireless device to precisely monitor fluid pressure, with the potential to estimate fluid physical properties, and a sensor-equipped robotic gripper to adaptively control the applied pressure and provide accurate dynamic feedback for manipulation tasks. Note that for our contact-dominated design, layered dielectrics utilized in this work exhibit no noticeable degradation down to millimeter bending radii. Other thin and/or high-k dielectrics with excellent robustness, such as two-dimensional layered dielectrics, are also expected to be introduced to further improve the mechanical robustness. The transduced pressure response could be further improved when low-dimensional TFTs with a higher on/off ratio are introduced. We expect that low-temperature solution processing techniques can be involved in our design for more scalable manufacture of high-performance sensing devices. We also expect that our contact-dominated sensing devices can be applied to monitor the pressure of diverse fluids, such as biofluids for medical purposes, and enable robots to perform more sophisticated manipulation tasks in conjunction with artificial intelligence technologies soon.

Methods

Analytical models and simulations

The detailed analytical models are presented in Supplementary Note 2. The electrical and mechanical simulations were conducted via FEM by Comsol Multiphysics 5.3. For the electrical simulations and analytical

models, the detailed parameters are listed below. For the microstructured dielectric design, the base length is 12 μm, the spacing is 12 μm, the tip length is 0.1 μm, and the dielectric constant is 2.5 for the elastomers and 25-μm-thick unstructured part. For the microstructured electrode design, the geometry of the microstructures is the same as that in the microstructured dielectric design, with a dielectric constant of 15 and a thickness of 50 nm. For the microstructured electrode with air gaps design, the parameters are the same as those of the microstructured electrode design except for a tip length of 1 μm. For our contact-dominated design, the dielectric parameters are the same as those of the microstructured electrode design, with hierarchical microstructures of base lengths of 100 μm, 50 μm, and 25 μm, spacing of 50 μm and 25 μm, and a tip length of 0.1 μm. The arrangement of the micropyramids is similar to that in Supplementary Fig. 2b. For the mechanical simulations, a two-order Mooney–Rivlin model was used with parameters of c_{10} and c_{01} of 1.5 MPa and 0.5 MPa, respectively, and a counter substrate with a Young's modulus of 1 GPa.

Fabrication of hybrid hierarchical microstructured electrodes

First, a PDMS/CNTs solution was produced by a mixture of CNTs solution (10 mg of multi-walled CNTs powder was dispersed in 2 g of isopropanol using bath sonication) and PDMS solution (1 g of PDMS from Dow Corning was mixed with 6 g of hexane). The self-patterned hierarchical microstructure was obtained by directly drop-casting the PDMS/CNTs solution on a silicon wafer with hydrophobic surface treatment and annealed in an oven at 120 °C for 2 hr. The hierarchical micropyramidal structure was obtained by casting the PDMS/CNTs solution on a silicon mould prepared by photolithography with hydrophobic surface treatment and annealed under the same conditions. Then, a 20-nm/50-nm-thick Ti/Au was deposited on the microstructures by electron beam evaporation (EBE, DE Technology Inc.). Finally, the hybrid microstructured layer was laminated on a thin PET substrate deposited with a 20-nm/60-nm-thick Ti/Au.

Fabrication of layered dielectrics

To fabricate the layered dielectrics of Y_2O_3/HfO_2, a 5-nm-thick Y_2O_3 layer was obtained by thermal oxidation of a 3-nm-thick Y at a temperature of 300 °C for 30 min, and then a 50-nm-thick HfO_2 layer was grown on the Y_2O_3 by atomic layer deposition (ALD, TFS 200, Beneq Oy). To fabricate the layered dielectrics of HfO_2/parylene, a 15-nm-thick HfO_2 layer was grown via ALD, followed by the deposition of a 200-nm-thick layer of parylene-C film via chemical vapor deposition (Specialty Coating Systems Inc.).

Fabrication of flexible floating-gate TFTs

The floating-gate CNT-based TFTs were fabricated on polyimide substrates. The local bottom gate and floating gate electrodes of Ti/Au (5 nm/25 nm) were defined by standard photolithography, EBE, and lift-off process. The dielectric of a 25-nm-thick HfO_2 was deposited by the ALD process at 90 °C. The highly pure semiconducting film of CNT networks was obtained by the dip-coating method and then patterned into desired stripes by photolithography and reactive ion etching (Minilock, Trion). The drain/source electrodes of Ti/Pd/Au (0.3 nm/40 nm/50 nm) were defined using the same process as the gate electrodes. An encapsulation layer of a 200-nm-thick parylene-C film was deposited on the device,e and the via-holes were opened by oxygen plasma etching with a power of 250 W for about 2 min.

Device characterizations

SEM images were taken by Sigma 300, Carl Zeiss Microscopy GmbH. The pressure loads were applied using a home-made force testing system consisting of a motorized vertical stage (GTS30V, Newport Inc.), a motorized test stand (ESM303, Mark-10 Inc.), and various force gauges (M7-012/10/50, Mark-10 Inc.). The capacitance was measured by a LCR meter (IM3536, Hioki Inc.). The electrical properties of TFTs were measured using a semiconductor parameter analyzer (Keithley 4200A-SCS, Tektronix) with a probe station (Summit 11000, Cascade Microtech). The electrical responses of integrated pressure sensors were measured by Agilent B2902B. The outputs of square waves for the readout circuits were collected by an oscilloscope (TBS1102X, Tektronix).

Robotic applications

Polyurethane tapes were used to encapsulate the sensor for robotic applications. For fluid physical property evaluation, the motorized robotic arm (UR5, Universal Robots) was used to perform the cyclic tests. The sensor was encapsulated with a thin polyethylene terephthalate (PET) protective layer during the test of fluid physical property evaluation. After each test, the encapsulated sensor was cleaned with detergent and/or water, and then dried. The output signal of the sensor (read out by our chip) recovers to almost the same initial value after the cleaning process (Supplementary Fig. 31), which indicates that the encapsulated sensor can be reused for accurate measurements. For accurate dynamic control for manipulative tasks, a servo-actuated robotic gripper (PGI-140-80, DH-Robotics) with two rubber cylinders was installed on the robotic arm. The speed of the gripper was adjusted according to the feedback from our sensor with the adaptive algorithm to control the pressure applied on the grasp objects.

Data availability

The data that support the findings of this study are available within the paper. Source data are provided with this paper, which have been deposited in Figshare at https://doi.org/10.6084/m9.figshare.29321147.v1.

References

1. Dahiya, R. S., Metta, G., Valle, M. & Sandini, G. Tactile Sensing—From Humans to Humanoids. *IEEE Trans. Robot.* **26**, 1–20 (2010).
2. Bartolozzi, C., Natale, L., Nori, F. & Metta, G. Robots with a sense of touch. *Nat. Mater.* **15**, 921–925 (2016).
3. Shih, B. et al. Electronic skins and machine learning for intelligent soft robots. *Sci. Robot.* **5**, eaaz9239 (2020).
4. Pierre, C. U. & Zhao, G. Recent progress in flexible pressure sensors based electronic skin. *Adv. Eng. Mater.* **23**, 2001187 (2021).
5. Heng, W., Solomon, S. & Gao, W. Flexible electronics and devices as human–machine interfaces for medical robotics. *Adv. Mater.* **34**, 2107902 (2022).
6. Shu, Q. et al. Flexible resistive tactile pressure sensors. *J. Mater. Chem. A* **12**, 9296–9321 (2024).
7. Kim, S. W. et al. Mechanically robust and linearly sensitive soft piezoresistive pressure sensor for a wearable human–robot interaction system. *ACS Nano* **18**, 3151–3160 (2024).
8. Cao, W. et al. Piezoresistive pressure sensor based on a conductive 3D sponge network for motion sensing and human–machine interface. *ACS Appl. Mater. Interfaces* **15**, 3131–3140 (2023).
9. Xu, C. et al. Flexible pressure sensors in human–machine interface applications. *Small* **20**, 2306655 (2024).
10. Min, S. et al. Clinical validation of a wearable piezoelectric blood-pressure sensor for continuous health monitoring. *Adv. Mater.* **35**, 2301627 (2023).
11. Zhang, Y. et al. Kirigami-inspired, three-dimensional piezoelectric pressure sensors assembled by compressive buckling. *npj Flex. Electron.* **8**, 23 (2024).
12. Bai, H. et al. Stretchable distributed fiber-optic sensors. *Science* **370**, 848–852 (2020).
13. Gan, J. et al. Flexible optical fiber sensing: materials, methodologies, and applications. *Adv. Devices Instrum.* **5**, 0046 (2024).

14. Lv, C. et al. Ultrasensitive linear capacitive pressure sensor with wrinkled microstructures for tactile perception. *Adv. Sci.* **10**, 2206807 (2023).
15. Ha, K. H. et al. Stretchable hybrid response pressure sensors. *Matter* **7**, 1895–1908 (2024).
16. Zhang, Y. et al. Ultrafast piezocapacitive soft pressure sensors with over 10 kHz bandwidth via bonded microstructured interfaces. *Nat. Commun.* **15**, 3048 (2024).
17. Liu, Q. et al. High-porosity foam-based iontronic pressure sensor with superhigh sensitivity of 9280 kPa^{-1}. *Nano-Micro Lett.* **14**, 1–12 (2022).
18. He, Y. et al. Creep-free polyelectrolyte elastomer for drift-free iontronic sensing. *Nat. Mater.* **23**, 1107–1114 (2024).
19. Puers, R. Capacitive sensors: When and how to use them. *Sens. Actuat. A-Phys.* **37**, 93–105 (1993).
20. Hammock, M. L. et al. 25th Anniversary Article: The Evolution of Electronic Skin (E-Skin): A Brief History, Design Considerations, and Recent Progress. *Adv. Mater.* **25**, 5997–6038 (2013).
21. Mannsfeld, S. C. B. et al. Highly sensitive flexible pressure sensors with microstructured rubber dielectric layers. *Nat. Mater.* **9**, 859–864 (2010).
22. Tee, B. C.-K. et al. Tunable Flexible Pressure Sensors using Microstructured Elastomer Geometries for Intuitive Electronics. *Adv. Funct. Mater.* **24**, 5427–5434 (2014).
23. Kang, S. et al. Highly Sensitive Pressure Sensor Based on Bioinspired Porous Structure for Real-Time Tactile Sensing. *Adv. Elect. Mater.* **2**, 1600356 (2016).
24. Chen, S., Zhuo, B. & Guo, X. Large Area One-Step Facile Processing of Microstructured Elastomeric Dielectric Film for High Sensitivity and Durable Sensing over Wide Pressure Range. *ACS Appl. Mater. Interfaces* **8**, 20364–20370 (2016).
25. Lee, K. et al. Rough-surface-enabled capacitive pressure sensors with 3D touch capability. *Small* **13**, 1700368 (2017).
26. Ruth, S. R. A. et al. Rational design of capacitive pressure sensors based on pyramidal microstructures for specialized monitoring of biosignals. *Adv. Funct. Mater.* **30**, 1903100 (2020).
27. Lee, S. et al. Nanomesh pressure sensor for monitoring finger manipulation without sensory interference. *Science* **370**, 966–970 (2020).
28. Joo, Y. et al. Silver nanowire-embedded PDMS with a multiscale structure for a highly sensitive and robust flexible pressure sensor. *Nanoscale* **7**, 6208–6215 (2015).
29. Li, T. et al. Flexible capacitive tactile sensor based on micropatterned dielectric layer. *Small* **12**, 5042–5048 (2016).
30. Shuai, X. et al. Highly sensitive flexible pressure sensor based on silver nanowires-embedded polydimethylsiloxane electrode with microarray structure. *ACS Appl. Mater. Interfaces* **9**, 26314–26324 (2017).
31. Cheng, W. et al. Flexible pressure sensor with high sensitivity and low hysteresis based on a hierarchically microstructured electrode. *IEEE Electron Device Lett.* **39**, 288–291 (2018).
32. Bae, G. Y. et al. Pressure/temperature sensing bimodal electronic skin with stimulus discriminability and linear sensitivity. *Adv. Mater.* **30**, 1803388 (2018).
33. Yang, J. et al. Flexible, tunable, and ultrasensitive capacitive pressure sensor with microconformal graphene electrodes. *ACS Appl. Mater. Interfaces* **11**, 14997–15006 (2019).
34. Ha, K. et al. Highly sensitive capacitive pressure sensors over a wide pressure range enabled by the hybrid responses of a highly porous nanocomposite. *Adv. Mater.* **33**, 2103320 (2021).
35. Zhang, Y. et al. Highly stable flexible pressure sensors with a quasi-homogeneous composition and interlinked interfaces. *Nat. Commun.* **13**, 1317 (2022).
36. Huang, Y.-C. et al. Sensitive pressure sensors based on conductive microstructured air-gap gates and two-dimensional semiconductor transistors. *Nat. Electron.* **3**, 59–69 (2020).
37. Schwartz, G. et al. Flexible polymer transistors with high pressure sensitivity for application in electronic skin and health monitoring. *Nat. Commun.* **4**, 1859 (2013).
38. Zang, Y. et al. Flexible suspended gate organic thin-film transistors for ultra-sensitive pressure detection. *Nat. Commun.* **6**, 6269 (2015).
39. Dagdeviren, C. et al. Conformable amplified lead zirconate titanate sensors with enhanced piezoelectric response for cutaneous pressure monitoring. *Nat. Commun.* **5**, 4496 (2014).
40. Popov, V. L., Heß, M. & Willert, E. *Handbook of Contact Mechanics: Exact Solutions of Axisymmetric Contact Problems*. (Springer, Berlin [Heidelberg], 2019).
41. Barber, J. R. & Billings, D. A. An approximate solution for the contact area and elastic compliance of a smooth punch of arbitrary shape. *Int. J. Mech. Sci.* **32**, 991–997 (1990).
42. Iglio, R. et al. Macroporous PDMS foam decorated with carbon nanotubes for conductometric pressure and strain sensors. in *2017 IEEE SENSORS* 1–3 (IEEE, Glasgow, 2017).
43. Lee, H. K. et al. Normal and shear force measurement using a flexible polymer tactile sensor with embedded multiple capacitors. *J. Microelectromech. Syst.* **17**, 934–942 (2008).
44. Núñez, C. G. et al. Energy-autonomous, flexible, and transparent tactile skin. *Adv. Funct. Mater.* **27**, 1606287 (2017).
45. Baek, S. et al. Flexible piezocapacitive sensors based on wrinkled microstructures: toward low-cost fabrication of pressure sensors over large areas. *RSC Adv.* **7**, 39420–39426 (2017).
46. Wan, S. et al. Graphene oxide as high-performance dielectric materials for capacitive pressure sensors. *Carbon* **114**, 209–216 (2017).
47. He, Z. et al. Capacitive pressure sensor with high sensitivity and fast response to dynamic interaction based on graphene and porous nylon networks. *ACS Appl. Mater. Interfaces* **10**, 12816–12823 (2018).
48. Liu, S.-Y., Lu, J.-G. & Shieh, H.-P. D. Influence of permittivity on the sensitivity of porous elastomer-based capacitive pressure sensors. *IEEE Sens. J.* **18**, 1870–1876 (2018).
49. Shi, H. et al. Screen-printed soft capacitive sensors for spatial mapping of both positive and negative pressures. *Adv. Funct. Mater.* **29**, 1809116 (2019).
50. Kim, J. et al. Soft wearable pressure sensors for beat-to-beat blood pressure monitoring. *Adv. Healthc. Mater.* **8**, 1900109 (2019).
51. Yang, J. C. et al. Microstructured porous pyramid-based ultrahigh sensitive pressure sensor insensitive to strain and temperature. *ACS Appl. Mater. Interfaces* **11**, 19472–19480 (2019).
52. Zeng, X. et al. Tunable, ultrasensitive, and flexible pressure sensors based on wrinkled microstructures for electronic skins. *ACS Appl. Mater. Interfaces* **11**, 21218–21226 (2019).
53. Xu, C. et al. A physicochemical-sensing electronic skin for stress response monitoring. *Nat. Electron.* **7**, 168–179 (2024).
54. Viry, L. et al. Flexible three-axial force sensor for soft and highly sensitive artificial touch. *Adv. Mater.* **26**, 2659–2664 (2014).
55. Wan, Y. et al. A highly sensitive flexible capacitive tactile sensor with sparse and high-aspect-ratio microstructures. *Adv. Elect. Mater.* **4**, 1700586 (2018).
56. Boutry, C. M. et al. A hierarchically patterned, bioinspired e-skin able to detect the direction of applied pressure for robotics. *Sci. Robot.* **3**, eaau6914 (2018).
57. Kim, H. et al. Transparent, flexible, conformal capacitive pressure sensors with nanoparticles. *Small* **14**, 1703432 (2018).
58. Ma, L. et al. A highly sensitive and flexible capacitive pressure sensor based on a micro-arrayed polydimethylsiloxane dielectric layer. *J. Mater. Chem. C.* **6**, 13232–13240 (2018).

59. Xiong, Y. et al. A flexible, ultra-highly sensitive and stable capacitive pressure sensor with convex microarrays for motion and health monitoring. *Nano Energy* **70**, 104436 (2020).
60. Zhang, Z. et al. Highly sensitive capacitive pressure sensor based on a micropyramid array for health and motion monitoring. *Adv. Elect. Mater.* **7**, 2100174 (2021).
61. Zhang, P., Zhang, J., Li, Y. & Huang, L. Flexible and high sensitive capacitive pressure sensor with microstructured electrode inspired by ginkgo leaf. *J. Phys. D: Appl. Phys.* **54**, 465401 (2021).
62. Zhang, J.-H. et al. Versatile self-assembled electrospun micropyramid arrays for high-performance on-skin devices with minimal sensory interference. *Nat. Commun.* **13**, 5839 (2022).
63. Joo, Y. et al. Highly sensitive and bendable capacitive pressure sensor and its application to 1 V operation pressure-sensitive transistor. *Adv. Elect. Mater.* **3**, 1600455 (2017).
64. Chang, Y. et al. First decade of interfacial iontronic sensing: from droplet sensors to artificial skins. *Adv. Mater.* **33**, 2003464 (2021).
65. Voorthuyzen, J. A., Bergveld, P. & Sprenkels, A. J. Semiconductor-based electret sensors for sound and pressure. *IEEE Trans. Elect. Insul.* **24**, 267–276 (1989).
66. Graz, I. et al. Flexible active-matrix cells with selectively poled bifunctional polymer-ceramic nanocomposite for pressure and temperature sensing skin. *J. Appl. Phys.* **106**, 034503 (2009).
67. Lai, S. et al. Ultralow voltage pressure sensors based on organic FETs and compressible capacitors. *IEEE Electron Device Lett.* **34**, 801–803 (2013).
68. Yeo, S. Y. et al. Highly sensitive flexible pressure sensors based on printed organic transistors with centro-apically self-organized organic semiconductor microstructures. *ACS Appl. Mater. Interfaces* **9**, 42996–43003 (2017).
69. Jang, J. et al. Mechanoluminescent, air-dielectric MoS_2 transistors as active-matrix pressure sensors for wide detection ranges from footsteps to cellular motions. *Nano Lett.* **20**, 66–74 (2020).
70. Seo, H. et al. Real-time in vivo monitoring of intraocular pressure distribution in the anterior chamber and vitreous chamber for diagnosis of glaucoma. *Sci. Adv.* **10**, eadk7805 (2024).
71. Germaná, S. et al. LAS acid reactive binder: Wettability and adhesion behaviour in detergent granulation. *Powder Technol.* **189**, 385–393 (2009).
72. Pang, X. D., Tan, H. Z. & Durlach, N. I. Manual discrimination of force using active finger motion. *Percept. Psychophys.* **49**, 531–540 (1991).
73. Liu, Y. et al. Ultrasensitive touch sensor for simultaneous tactile and slip sensing. *Adv. Mater.* **36**, 2313857 (2024).

Acknowledgements

This work was supported by the National Natural Science Foundation of China (Grant no. 62304011 for C. M.) and China Postdoctoral Science Foundation (Grant no. 2022TQ0003 for C.M.), National Key R&D Program of China (Grant No. 2021YFA1202904 and 2022YFB4401603 for Y. H.).

Author contributions

C.M., Y.H. and L.-M. P. conceived the experiments. C.M. performed device design and fabrication, electrical measurements, robotic applications, and data analysis. H.Y. and X.J. contributed to the optimization of layered dielectrics and sensors. X.S., Y.L., L.Q., L.G. and W.H. contributed to the robotic experiments. Y.C., F.X., and G.L. contributed to the design and fabrication of CNT-TFTs. X.C. and X.L. prepared the CNT solutions and thin films. C.M. and Y.H. co-wrote the paper, and all authors discussed the results and commented on the manuscript.

Competing interests

The authors declare no competing interests.

Additional information

Supplementary information The online version contains supplementary material available at https://doi.org/10.1038/s41467-025-63018-9.

Correspondence and requests for materials should be addressed to Lian-Mao Peng or Youfan Hu.

Peer review information *Nature Communications* thanks Dawen Zeng, and the other, anonymous, reviewer(s) for their contribution to the peer review of this work. A peer review file is available.